

Corrosion Behaviors of AA5083 and AA6061 in Artificial Seawater: Effects of Cl^- , HSO_3^- and Temperature

Zhan Zhang^{1,2}, Zhilong Xu², Jine Sun², Meiting Zhu², Qiong Yao³, Dongjiu Zhang³, Bowei Zhang¹, Kui Xiao¹, Junsheng Wu^{1,2,*}

¹ Institute for advanced materials and technology, University of Science and Technology Beijing, Beijing 100083, China;

² Department of materials science and engineering, Tianjin College, University of Science and Technology Beijing, Tianjin 301830, China;

³ Key Laboratory of Space Launching Site Reliability Technology, Haikou 571000, China

*E-mail: wujis@ustb.edu.cn

Received: 22 August 2019 / Accepted: 30 October 2019 / Published: 31 December 2019

The electrochemical character of intermetallic inclusions plays a crucial role in the corrosion behaviors of aluminum alloys. The Volta potential of the intermetallic inclusions in AA5083 and AA6061 was investigated. Furthermore, the effects of Cl^- , HSO_3^- and temperature on the corrosion behaviors of AA5083 and AA6061 were studied. The microstructure and composition of the intermetallic inclusion were characterized by scanning electron microscope (SEM) and energy-dispersive spectroscopy (EDS). The Volta potential was analyzed by scanning Kelvin probe force microscopy (SKPFM). The alternate immersion test and potentiodynamic polarization curve test were used to evaluate the corrosion resistance. The results show that $\text{Al}_6(\text{Fe}, \text{Mn})$ has a higher potential than that of the AA5083 matrix, resulting in the dissolution of the surrounding matrix. The Mg_2Si phase has a lower potential compared to that of the matrix, leading to self-dissolution and dealloying. In addition, the AlFeSi phase has a higher potential and the Mg_2Si phase has a lower potential than that of the AA6061 matrix. Pitting corrosion occurs on the surface of both the AA5083 and AA6061 after the alternate immersion test. Increases in the concentration of Cl^- and HSO_3^- accelerates the corrosion of the aluminum alloys. The effect of temperature is affected by both the chemical reactivity and passivation ability. In the same conditions, the AA5083 has superior corrosion resistance to that of the AA6061, which is related to the potential difference between the matrix and intermetallic inclusions.

Keywords: aluminum alloys, intermetallic inclusion, Volta potential, corrosion behavior

1. INTRODUCTION

Aluminum alloys are widely used in the shipbuilding industry due to their high strength to weight ratio, superior conductivity and excellent corrosion resistance [1,2]. AA5083 and AA6061 are two

typical kinds of aluminum alloys for ship applications [3–6]. The presence of intermetallic inclusions enhances the mechanical properties of the aluminum alloy, but simultaneously reduces the corrosion resistance. The main types of intermetallic inclusions in the AA5083 are (Fe, Mn)-rich phases and Mg-rich phases [7,8], and the main types of intermetallic inclusions in the AA6061 are (Fe, Si)-rich phases and Mg-rich phases [9,10].

The microstructure of materials is closely related to corrosion behavior. Scanning Kelvin probe force microscopy (SKPFM), as an emerging microscopic approach, has been successfully used in the field of corrosion [11–13]. The measured Volta potential difference in air can be correlated with the OCP measured in liquid [14]. Therefore, SKPFM can be applied to investigate the electrochemical behavior of different metals [15–18]. In recent years, the intermetallic inclusions in the AA2024 and AA7075 have been studied by SKPFM [19–22]. However, the investigation of the intermetallic inclusions in the AA5083 and AA6061 by SKPFM is rarely reported.

Corrosion behavior of the aluminum alloy in seawater is affected by many factors [23–25]. Chloride ions have a strong corrosive effect on metals, which can destroy passive films, and can eventually cause localized corrosion [26]. HSO_3^- is formed by SO_2 dissolved in seawater, which can accelerate the corrosion of aluminum alloys [27,28]. In addition, the temperature is also one of the crucial factors affecting the corrosion behavior of aluminum alloys. It is necessary to study the effects of different factors on the corrosion behaviors of AA5083 and AA6061.

In the present work, the microstructure of the AA5083 and AA6061 and the Volta potential of the intermetallic inclusions are investigated by SEM-BSE and SKPFM. In addition, the effects of Cl^- , HSO_3^- and temperature on the corrosion behaviors of AA5083 and AA6061 are studied by an alternate immersion test and a potentiodynamic polarization curves test.

2. EXPERIMENTS

2.1 Experimental material

The experimental material was the 5083 and 6061 aluminum alloys. The chemical composition(wt.%) of the AA5083 was: Zn 0.01, Mg 4.76, Cr 0.1, Si 0.1, Fe 0.31, Cu 0.026, Mn 0.52, Ti 0.029, and Al balance. The chemical composition(wt.%) of the AA6061 was: Zn 0.012, Mg 1.18, Cr 0.12, Si 0.64, Fe 0.32, Cu 0.25, Mn 0.1, Ti 0.011, and Al balance.

2.2 Morphology and Volta potential analysis

For the microstructural characterization and Volta potential analysis with SEM and AFM, the samples with a size of $\phi 10 \text{ mm} \times 3 \text{ mm}$ were wet ground with SiC papers up to 4000-grit, and then mechanically polished using a $0.5 \mu\text{m}$ diamond paste. After mechanical polishing, the samples were vibrationally polished again by employing a $0.02 \mu\text{m}$ paste to remove polishing scratches, followed by sequential cleaning with acetone, deionized water, and anhydrous alcohol.

The surface morphologies of the samples were observed by scanning electron microscopy (FEI

Quanta 250). The local components of intermetallic particles were analyzed by energy-dispersive spectroscopy (EDS). Volta potential images were taken using an atomic force microscope (Burker Multimode 8). All mappings were performed in air at room temperature with relative humidity between 20 and 30% [29]. The AFM used a pyramidal single crystal silicon probe tip coated by conductive PtIr. For Volta potential mapping, the lift scan height was approximately 80 nm. Topography and Volta potentials were scanned with a square area of $20\ \mu\text{m}\times 20\ \mu\text{m}$ and a scan frequency rate of 0.1 Hz.

2.3 Alternate immersion test

The samples with a size of $30\ \text{mm}\times 40\ \text{mm}\times 3\ \text{mm}$ were ground with SiC papers up to 1000 grit for alternate immersion tests. In accordance with ASTM G44 Practice, all the samples were immersed in a solution for a period of 10 min, after which it was exposed to air for 50 min. To study the effect of Cl^- concentration, solutions with concentrations of 3.5 wt.%, 5 wt.% and 7 wt.% NaCl were used in the alternate immersion experiment, and the temperature was 25 °C. To study the effect of HSO_3^- concentration, the solutions were 3.5 wt.% NaCl with 0 M, 0.01 M and 0.02 M NaHSO_3 , and the temperature was 25 °C. To study the effect of temperature, the immersion experiment was conducted with 3.5 wt.% NaCl solution at 25 °C, 35 °C and 45 °C. The corrosion morphology was observed by stereoscopic microscope.

2.4 Polarization curve test

The samples were machined into a square sheet with dimensions of $10\times 10\times 3\ \text{mm}$, and then sequentially wet ground to 2000 grit SiC paper, degreased with alcohol, cleaned in water, and finally dried in cold air. An electrochemical workstation (Autolab, PGSTAT302N) was used to test the polarization curve with a standard three-electrode system, in which a saturated calomel electrode (SCE), a platinum electrode and a sample were used as a reference, counter, and working electrode, respectively. The temperature of the solution was controlled by water bath heating. Potentiodynamic polarization measurements were performed at a scan rate of 0.5 mV/s.

To study the influence of Cl^- concentration, the electrochemical test solution was treated with NaCl solution at concentrations of 1 wt.%, 2 wt.%, 3.5 wt.%, 5 wt.%, and 7 wt.%, at a temperature of 25 °C. To study the effect of HSO_3^- concentration, electrochemical tests were performed in 3.5 wt.% NaCl with 0 M, 0.005 M, 0.01 M, 0.02 M, and 0.05 M NaHSO_3 at a temperature of 25 °C. To study the effect of temperature, the tests were conducted in a 3.5% NaCl solution at temperatures of 25 °C, 35 °C, 45 °C, 50 °C, 55 °C, and 65 °C.

3. RESULTS AND DISCUSSION

3.1 Microstructure and Volta potential analysis

Fig. 1(a) shows the SEM-BSE image of 5083 aluminum alloy. AA5083 includes two types of

intermetallic inclusions, the white phase (e.g., square A) and the grey phase (e.g., square B). The composition of the two types of intermetallic inclusions on squares A and B were analyzed by EDS (Fig. 1(b) and 1(c)). As shown in Fig. 1(b), the intermetallic inclusion in square A mainly contains Al, Fe and Mn and should be $Al_6(Fe, Mn)$. As shown in Fig. 1(c), the intermetallic inclusion in square B mainly includes Mg and Si and should be Mg_2Si [8].

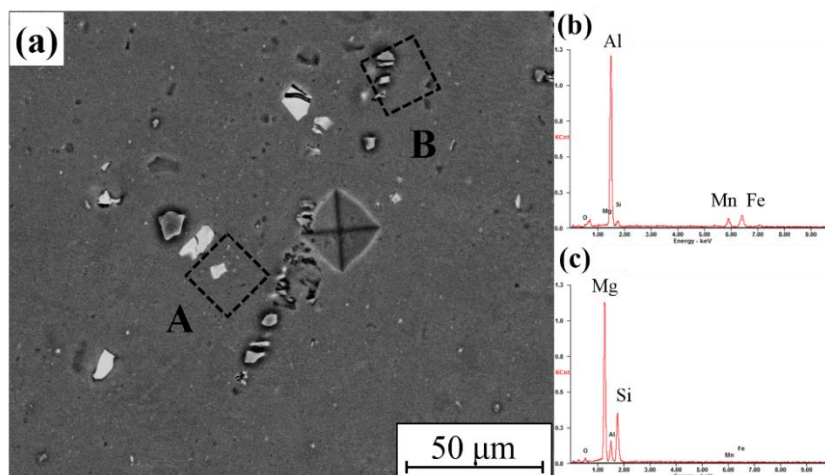


Figure 1. (a) SEM-BSE image of the AA5083 surface; (b) the EDS result of the intermetallic inclusion in square A; and (c) the EDS result of the intermetallic inclusion in square B.

Fig. 2(a) presents the SEM-BSE image of 6061 aluminum alloy. The main types of intermetallic inclusions are the white phase (e.g., square C) and the grey phase (e.g., square D). The composition of the two types of intermetallic inclusions in squares C and D were analyzed by EDS (Fig. 2(b) and 2(c)). As shown in Fig. 2(b), the intermetallic inclusion in square C mainly contains Al, Fe and Si and should be $AlFeSi$. As shown in Fig 2(c), the intermetallic inclusion in square D mainly includes Mg and Si and should be Mg_2Si [30].

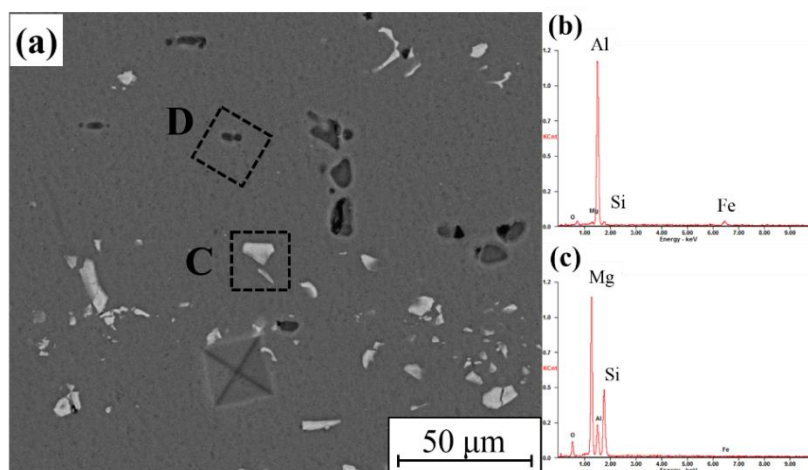


Figure 2. (a) SEM-BSE images of the AA6061 surface; (b) the EDS result of the intermetallic inclusion in square C; and (c) the EDS result of the intermetallic inclusion in square D.

Positioning was performed using a microhardness tester to further investigate the Volta potential using the SKPFM technique. Fig. 3(a) shows the SKPFM image of $\text{Al}_6(\text{Fe, Mn})$ from square A shown in Fig. 1. The $\text{Al}_6(\text{Fe, Mn})$ phase is brighter, indicating that the Volta potential of the $\text{Al}_6(\text{Fe, Mn})$ is higher than the matrix. According to the result of line scanning (Fig.3(b)), the Volta potential of $\text{Al}_6(\text{Fe, Mn})$ is approximately 500 mV higher compared to that of the Al matrix, which is similar to the KA's results [8]. Fig. 3(c) shows the SKPFM image of Mg_2Si from square B shown in Fig. 1. According to the results of line-scanning (Fig. 3(d)), the Volta potential of Mg_2Si is approximately 100 mV lower than that of the Al matrix.

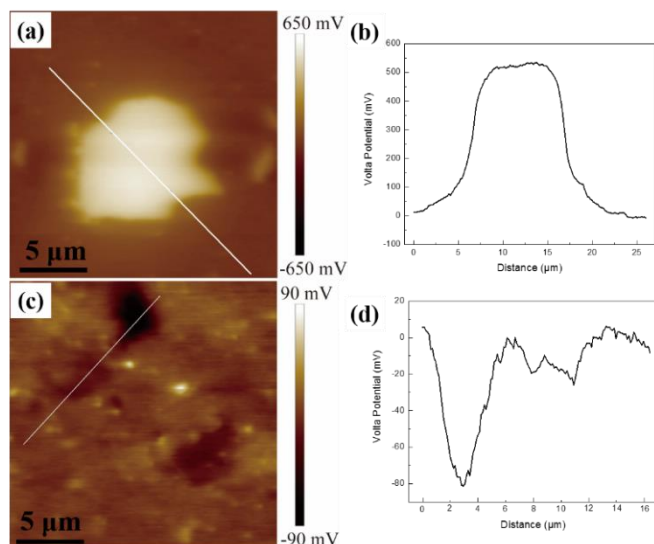


Figure 3. (a) SKPFM image of $\text{Al}_6(\text{Fe, Mn})$ from square A shown in Fig. 1; (b) Volta potential line scanning of (a); (c) SKPFM image of the Mg_2Si from square B shown in Fig. 1; and (d) Volta potential line scanning of (c).

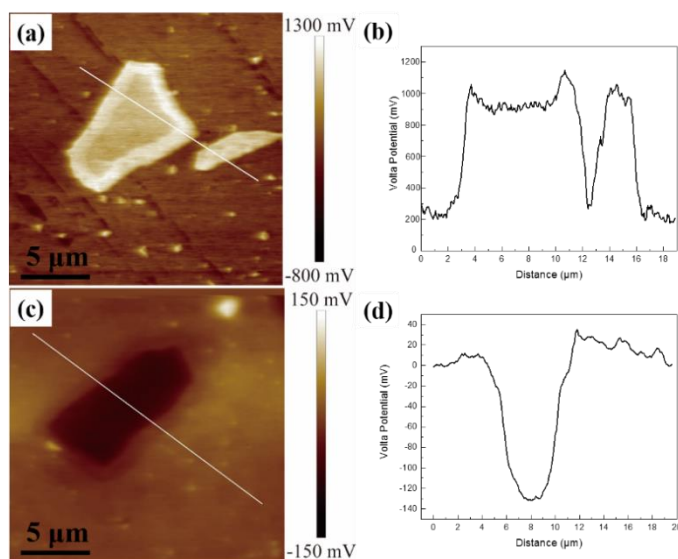


Figure 4. (a) SKPFM image of AlFeSi from square C shown in Fig. 2; (b) Volta potential line scanning of (a); (c) SKPFM image of Mg_2Si from square D shown in Fig. 2; (d) Volta potential line scanning of (c).

Fig. 4(a) presents the SKPFM image of AlFeSi phase from square C in Fig. 2. The AlFeSi phase is brighter, indicating that the Volta potential of the AlFeSi is higher than that of the matrix. According to the result of line scanning (Fig. 4(b)), the Volta potential of AlFeSi is approximately 800 mV higher than that of the Al matrix. Fig. 4(c) shows the SKPFM image of Mg₂Si from square D shown in Fig. 2. According to the result of line scanning (Fig. 4(d)), the Volta potential of Mg₂Si is approximately 130 mV lower than that of the Al matrix. This result is consistent with the Andreatta's conclusion [21].

The intermetallic inclusions with higher Volta potential compared to the matrix, such as Al₆(Fe, Mn) and AlFeSi, play a cathodic role, resulting in the dissolution of the surrounding matrix. In addition, the intermetallic inclusions with lower Volta potential compared to the matrix, such as Mg₂Si, act as an anode, leading to self-dissolution and dealloying. Therefore, the relative difference in the potential between the intermetallic inclusions and the matrix determines the corrosion resistance of the aluminum alloys.

3.2 Effect of Cl⁻ concentration

Fig. 5 shows the effect of different Cl⁻ concentrations on the corrosion morphology of AA5083 and AA6061 after the alternate immersion test for 30 days. It can be seen from Fig. 5 that the pitting density increases with the increase in Cl⁻ concentration. When the concentration of NaCl increases to 7 wt.%, the pits gradually expand and partially connect into larger defects. At the same concentration of Cl⁻, the corrosion area of AA6061 is larger than that of AA5083, indicating that AA5083 has better corrosion resistance than AA6061.

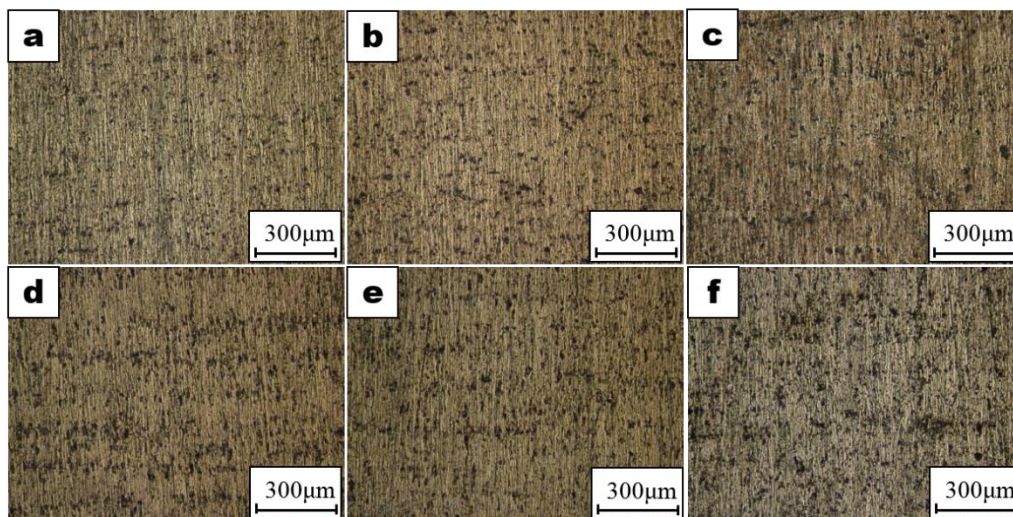


Figure 5. Corrosion morphology of aluminum alloys with different concentrations of NaCl after the alternate immersion test for 30 days: (a) AA5083, 3.5%; (b) AA5083, 5%; (c) AA5083, 7%; (d) AA6061, 3.5%; (e) AA6061, 5%; (f) AA6061, 7%.

Fig. 6 shows the potentiodynamic polarization curves of aluminum alloys at different concentrations of Cl⁻. Aluminum alloy dissolves without the formation of a passive film during the

anodic reaction [31]. The corrosion current density (I_{corr}) and corrosion potential (E_{corr}) are calculated from the intercept of the Tafel slopes tabulated in Table 1. As the Cl^- concentration increases, E_{corr} decreases and I_{corr} increases, indicating that the Cl^- increase accelerates the corrosion of aluminum alloys. In addition, at the same Cl^- concentration, the I_{corr} of AA5083 is smaller than the I_{corr} of AA 6061, indicating that the corrosion resistance of AA5083 is better than that of AA6061.

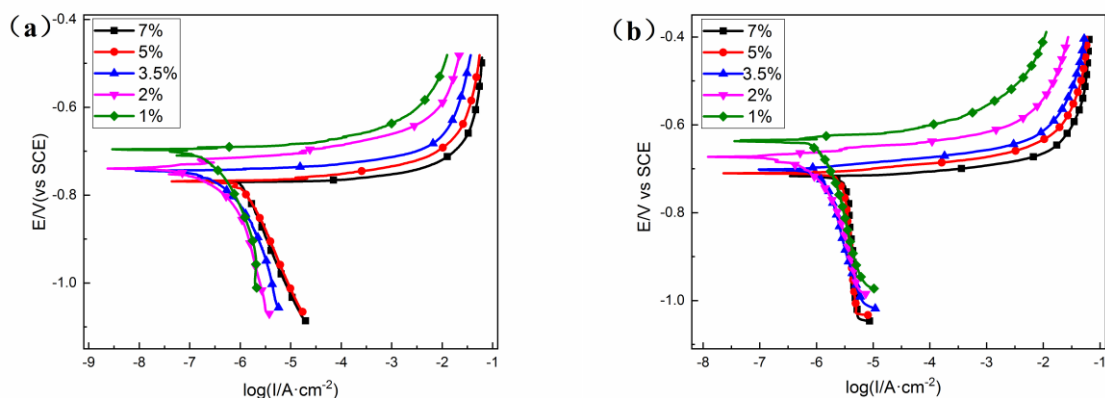


Figure 6. Potentiodynamic polarization curves of aluminum alloys with different concentrations of NaCl: (a) AA5083 and (b) AA6061.

Table 1. Electrochemical parameters obtained from the potentiodynamic polarization curves of aluminum alloys with different concentrations of Cl^- .

materials	concentration of NaCl/wt. %	E_{corr}/V	$I_{\text{corr}}/\mu\text{A}\cdot\text{cm}^{-2}$
AA5083	1	-0.697	0.228
AA5083	2	-0.740	0.183
AA5083	3.5	-0.743	0.797
AA5083	5	-0.769	1.021
AA5083	7	-0.771	1.132
AA6061	1	-0.637	0.965
AA6061	2	-0.673	0.608
AA6061	3.5	-0.702	1.326
AA6061	5	-0.718	1.500
AA6061	7	-0.717	3.376

3.3 Effect of HSO_3^- concentration

Fig. 7 shows the effect of different HSO_3^- concentrations on the corrosion morphology of AA5083 and AA6061 after the alternate immersion test for 30 days. As shown in Fig. 7, pitting corrosion occurs on the surface of the aluminum alloy, and the addition of NaHSO_3 leads to an increase in the corrosion area. Meanwhile, the corrosion area increases with increasing NaHSO_3 content. Comparing

AA5083 and AA6061, the corrosion degree of AA6061 is more serious than that of AA5083 at the same concentration.

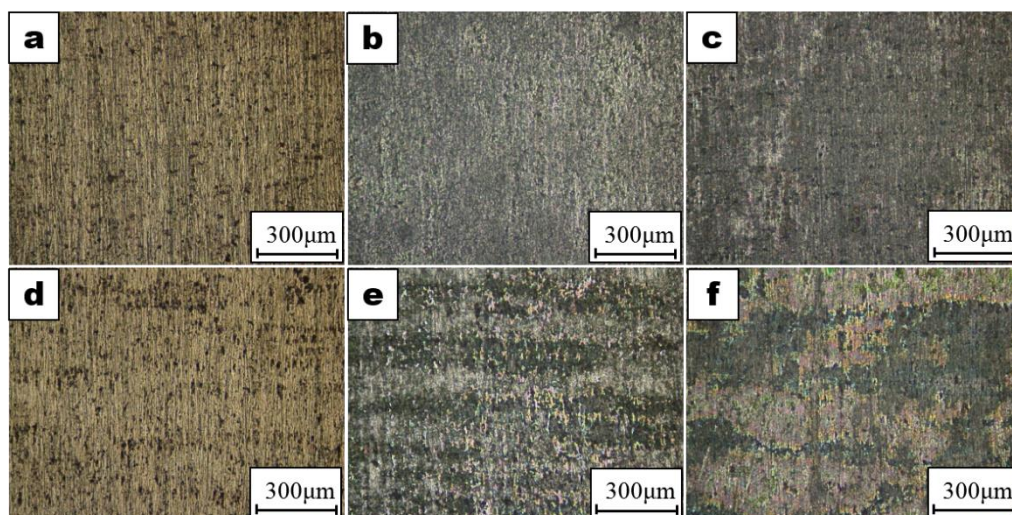


Figure 7. Corrosion morphology of aluminum alloys with different NaHSO_3 concentrations after the alternate immersion test for 30 days: (a) AA5083, 0 M; (b) AA5083, 0.01M; (c) AA5083, 0.02M; (d) AA6061, 0 M; (e) AA6061, 0.01M; (f) AA6061, 0.02M.

Fig. 8 shows the potentiodynamic polarization curves of aluminum alloys with different concentrations of NaHSO_3 . The corrosion current density (I_{corr}) and corrosion potential (E_{corr}) are calculated from the intercept of the Tafel slopes tabulated in Table 2. As the HSO_3^- concentration increases, E_{corr} slightly changes and I_{corr} increases, indicating that the HSO_3^- increase accelerates the corrosion of the aluminum alloys [32]. Besides, at the same HSO_3^- concentration, the I_{corr} of AA5083 is similar to the I_{corr} of the AA6061, indicating that the corrosion resistance of AA5083 is comparable to that of AA6061 in this environment. The HSO_3^- dissolves in seawater to form an acidic environment, which is damaging to the protective passive film.

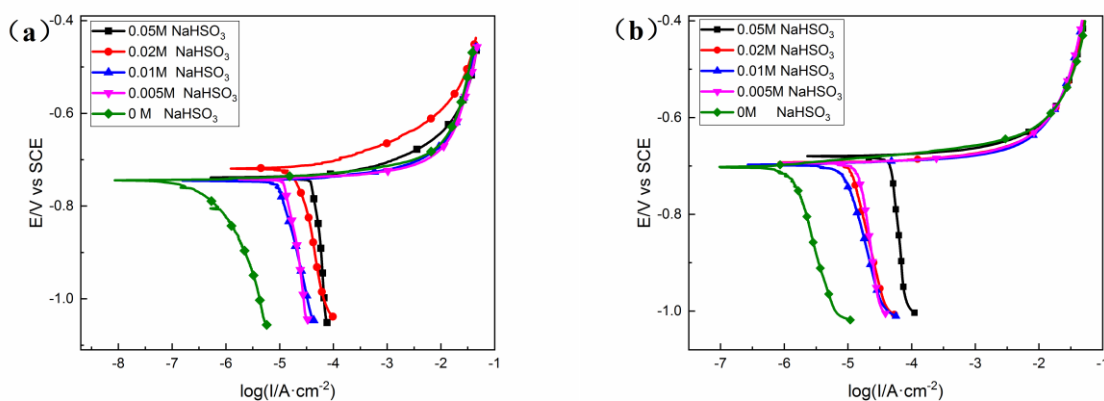


Figure 8. Potentiodynamic polarization curves of the aluminum alloys with different HSO_3^- concentrations: (a) AA5083 and (b) AA6061.

Table 2. Electrochemical parameters obtained from the potentiodynamic polarization curves of aluminum alloys with different NaHSO₃ concentrations.

materials	concentration of NaCl/wt. %	concentration of NaHSO ₃ /mol·L ⁻¹	E _{corr} /V	I _{corr} /μA·cm ⁻²
AA5083	3.5	0	-0.743	0.797
AA5083	3.5	0.005	-0.742	11.400
AA5083	3.5	0.01	-0.745	8.905
AA5083	3.5	0.02	-0.719	16.920
AA5083	3.5	0.05	-0.737	37.182
AA6061	3.5	0	-0.702	1.326
AA6061	3.5	0.005	-0.694	13.914
AA6061	3.5	0.01	-0.697	8.054
AA6061	3.5	0.02	-0.693	11.556
AA6061	3.5	0.05	-0.680	46.008

3.4 Effect of temperature

Fig. 9 shows the effect of different temperatures on the corrosion morphology of AA5083 and AA6061 after the alternate immersion test for 30 days. When the solution temperature is 35°C, the metal loses metallic luster. Simultaneously, the number of pits on AA5083 increases, and the pits on AA6061 become larger and connect into larger defects. When the solution temperature increases to 45 °C, the surface of the two aluminum alloys is grey, and a small number of white corrosion products are distributed on the surface of AA5083 and AA6061. By comparing Fig.9(c) and Fig. 9(f), the corrosion products of AA6061 are more than those of AA5083.

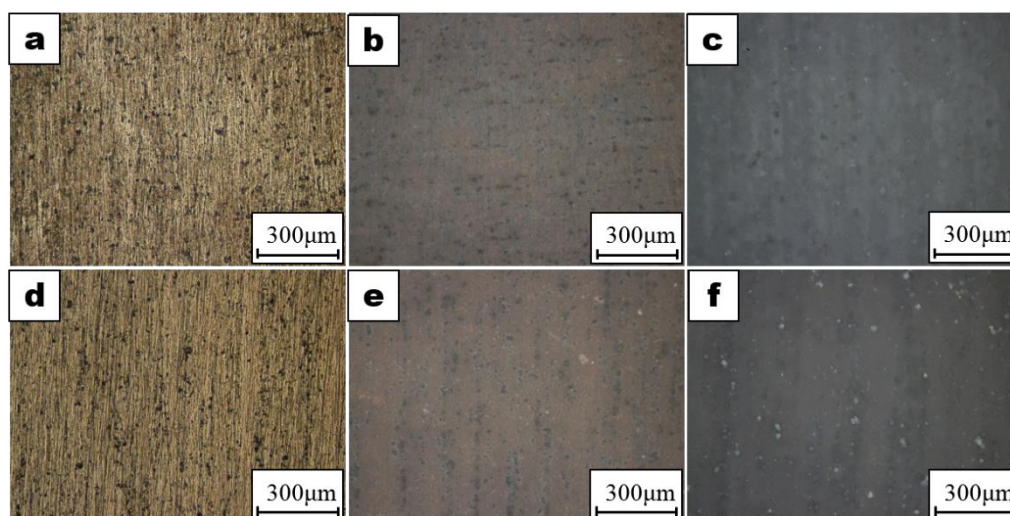


Figure 9. Corrosion morphology of aluminum alloys with different temperatures after the alternate immersion test for 30 days: (a)AA5083, 25 °C; (b) AA5083, 35 °C; (c) AA5083, 45 °C; (d) AA6061, 25 °C; (e) AA6061, 35 °C; (f) AA6061, 45 °C.

Fig. 10 shows the potentiodynamic polarization curves of AA5083 and AA6061 at different temperatures. The electrochemical parameters obtained from the potentiodynamic polarization curves of aluminum alloys at different temperatures are shown in Table 3. As the temperature increases from 25 °C to 45 °C, the corrosion rate gradually increases. The I_{corr} begins to decrease at 50 °C, and passivation occurs at 55 °C. The reason is that the increase in temperature results in an increase in chemical reactivity. However, the binding ability between the surface of the aluminum alloys and dissolved oxygen improves with increasing temperature, resulting in the improvement of passivation ability and a subsequent decrease in the corrosion rate [33]. Therefore, the corrosion rate is determined by the synergistic effect between the chemical reactivity and passivation ability. At the same temperature, the I_{corr} of AA6061 is higher than that of AA5083, which indicates that the corrosion resistance of AA5083 is superior to that of AA6061.

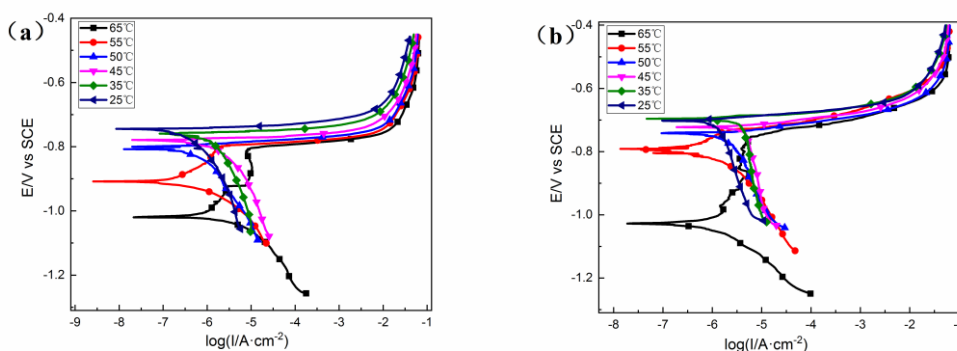


Figure 10. Potentiodynamic polarization curves of the aluminum alloys at different temperatures: (a) AA5083 and (b) AA6061.

Table 3. Electrochemical parameters obtained from the potentiodynamic polarization curves of aluminum alloys at different temperatures

materials	Temperature/°C	E_{corr}/V	$I_{\text{corr}}/\mu\text{A}\cdot\text{cm}^{-2}$
AA5083	25	-0.743	0.797
AA5083	35	-0.759	1.490
AA5083	45	-0.779	2.851
AA5083	50	-0.800	1.516
AA5083	55	-0.908	-
AA5083	65	-1.019	-
AA6061	25	-0.702	1.326
AA6061	35	-0.696	3.768
AA6061	45	-0.723	4.546
AA6061	50	-0.739	3.490
AA6061	55	-0.793	-
AA6061	65	-1.028	-

4. CONCLUSIONS

The electrochemical character of different intermetallic inclusions in the AA5083 and AA 6061 were investigated by SKPFM. For AA5083, the Volta potential of $Al_6(Fe, Mn)$ is approximately 500 mV higher than that of the aluminum matrix, and the Volta potential of Mg_2Si is approximately 100 mV lower than that of the matrix. For AA6061, the Volta potential of $AlFeSi$ is approximately 800 mV higher than that of the aluminum matrix, and the Volta potential of Mg_2Si is approximately 130 mV lower than that of the matrix. The micro-battery that forms from the potential difference between the intermetallic inclusions and the matrix is an important factor affecting the corrosion resistance of the material.

Pitting corrosion occurred on the surface of both the AA5083 and AA6061 after the alternate immersion test. The increase in Cl^- destroys the formation of a passive film. The addition of HSO_3^- leads to an acidic solution. The increase in the concentration of Cl^- and HSO_3^- accelerates the corrosion of the aluminum alloy. The effect of temperature is affected by both the chemical reactivity and passivation ability. In the same conditions, the AA5083 has superior corrosion resistance to that of AA6061, which is consistent with the results of the SKPFM.

ACKNOWLEDGMENTS

This work was supported by the National Natural Science Foundation of China (Grant No. 51771027), the Fundamental Research Funds for the Central Universities (Grant No. FRF-BD-18-019A), and the National Key Research and Development Program of China (Grant No. 2017YFB0702100).

References

1. R. Ly, K.T. Hartwig, H. Castaneda, *Corros. Sci.*, 139 (2018) 47.
2. Q. Zhao, *Int. J. Electrochem. Sci.*, 14 (2019) 8228.
3. A. Aballe, M. Bethencourt, F.J. Botana, M.J. Cano, M. Marcos, *Corros. Sci.*, 43 (2001) 1657.
4. S. Benedictus-deVries, A. Bakker, G.C.A.M. Janssen, H. de Wit, *J. Eng. Mater. Technol.*, 126 (2004) 199.
5. A.G.G. Gutiérrez, P.J. Sebastian, L.M. Cacho, E.B. Arco, J. Campos, A. Baron, *Int. J. Electrochem. Sci.*, 13 (2018) 3958.
6. N.C.T. Martins, T. Moura e Silva, M.F. Montemor, J.C.S. Fernandes, M.G.S. Ferreira, *Electrochim. Acta*, 53 (2008) 4754.
7. L. Tan, T.R. Allen, *Corros. Sci.*, 52 (2010) 548.
8. K.A. Yasakau, M.L. Zheludkevich, S. V. Lamaka, M.G.S. Ferreira, *Electrochim. Acta*, 52 (2007) 7651.
9. N.C.W. Kuijpers, W.H. Kool, P.T.G. Koenis, K.E. Nilsen, I. Todd, S. Van der Zwaag, *Mater. Charact.*, 49 (2002) 409.
10. Z. Zhang, W. Rong, J. Wu, T. Zhang, Y. Wang, K. Huang, B. Zhang, Y. He, *Surf. Coatings Technol.*, 370 (2019) 130.
11. M. Rohwerder, F. Turcu, *Electrochim. Acta*, 53 (2007) 290.
12. T. Pan, *J. Appl. Electrochem.*, 42 (2012) 1049.
13. J. Sun, X. Li, Y. Sun, Y. Jiang, J. Li, *Int. J. Electrochem. Sci.*, 13 (2018) 11607.
14. P. Schmutz, *J. Electrochem. Soc.*, 145 (2006) 2285.
15. M.L. Zheludkevich, K.A. Yasakau, S.K. Poznyak, M.G.S. Ferreira, *Corros. Sci.*, 47 (2005) 3368.

16. N. Sathirachinda, R. Pettersson, S. Wessman, U. Kivisäkk, J. Pan, *Electrochim. Acta*, 56 (2011) 1192.
17. C. Senöz, A. Maljusch, M. Rohwerder, W. Schuhmann, *Electroanalysis*, 24 (2012) 239.
18. M. Sarvghad-Moghaddam, R. Parvizi, A. Davoodi, M. Haddad-Sabzevar, A. Imani, *Corros. Sci.*, 79 (2014) 148.
19. K.A. Yasakau, M.L. Zheludkevich, M.G.S. Ferreira, *Mater. Sci. Forum*, 587 (2009) 405.
20. A. Arutunow, A. Zieliński, M.T. Tobiszewski, *Anti-Corrosion Methods Mater.*, 60 (2013) 67.
21. F. Andreatta, H. Terryn, J.H.W. de Wit, *Corros. Sci.*, 45 (2003) 1733.
22. F. Andreatta, H. Terryn, J.H.W. De Wit, *Electrochim. Acta*, 49 (2004) 2851.
23. H. Ezuber, A. El-Houd, F. El-Shawesh, *Mater. Des.*, 29 (2008) 801.
24. M. Sakairi, R. Sasaki, A. Kaneko, Y. Seki, D. Nagasawa, *Electrochim. Acta*, 131 (2014) 123.
25. A. Pardo, M.C. Merino, A.E. Coy, R. Arrabal, F. Viejo, E. Matykina, *Corros. Sci.*, 50 (2008) 823.
26. D. Kong, X. Ni, C. Dong, L. Zhang, C. Man, J. Yao, K. Xiao, X. Li, *Electrochim. Acta*, 276 (2018) 293.
27. X. Yang, C. Du, H. Wan, Z. Liu, X. Li, *Appl. Surf. Sci.*, 458 (2018) 198.
28. H. Ma, Z. Liu, C. Du, X. Li, Z. Cui, *Mater. Sci. Eng. A*, 650 (2016) 93.
29. L.Q. Guo, X.M. Zhao, Y. Bai, L.J. Qiao, *Appl. Surf. Sci.*, 258 (2012) 9087.
30. X. Zhan, J. Chen, J. Liu, Y. Wei, J. Zhou, Y. Meng, *Mater. Des.*, 99 (2016) 449.
31. M. Zhu, C.W. Du, X.G. Li, Z.Y. Liu, *Mater. Corros.*, 66 (2015) 494.
32. K. Xiao, P. Yi, L. Yan, Z. Bai, C. Dong, P. Dong, X. Gao, *Materials*, 10 (2017) 762.
33. F.M. Khoshnaw, R.H. Gardi, *Mater. Corros.*, 58 (2007) 345.